

Huaichun Wu, Linda A. Hinnov, Shihong Zhang, Ganqing Jiang, Tianshui Yang, Haiyan Li, Dangpeng Xi, Xiaojuan Ma, and Chengshan Wang, 2022, Continental geological evidence for Solar System chaotic behavior in the Late Cretaceous: GSA Bulletin, <https://doi.org/10.1130/B36340.1>.

Supplemental Material

Figure S1. Long term trends in the Th and ostracode shell abundance series.

Figure S2. 2π multi-tapered power spectral analysis of paleoclimate proxy records from the SK-1s core.

Figure S3. 2π MTM power spectrum (upper) and FFT spectrogram (lower) of 405-k.y.-tuned Th time series of the SK-1s core, with an 800 k.y. sliding window and 5 k.y. step.

Figure S4. 2π MTM power spectrum and FFT spectrogram of 405-k.y.-tuned ostracode abundance time series, with a 1000 k.y. sliding window and 10 k.y. step.

Figure S5. Comparison of amplitude modulations in the 405 k.y.-tuned Th log and ostracode shell abundance time series at short and long orbital eccentricity frequencies.

Figure S6. Amplitude modulations expressed in the short orbital eccentricity and 405-k.y. long orbital eccentricity time series from the theoretical astronomical solutions of La2004 (Laskar et al., 2004), La2010d (Laskar et al., 2011a) and La2011 (Laskar et al., 2011b).

Table S1. Frequencies in Earth's short orbital eccentricity and obliquity variations influenced by secular frequencies s_3 , s_4 , g_3 and g_4 .

Table S2. Phasing of La2004 solution, and SB (Th and ostracode shell abundance) and WIS (FMI) proxy modulations.

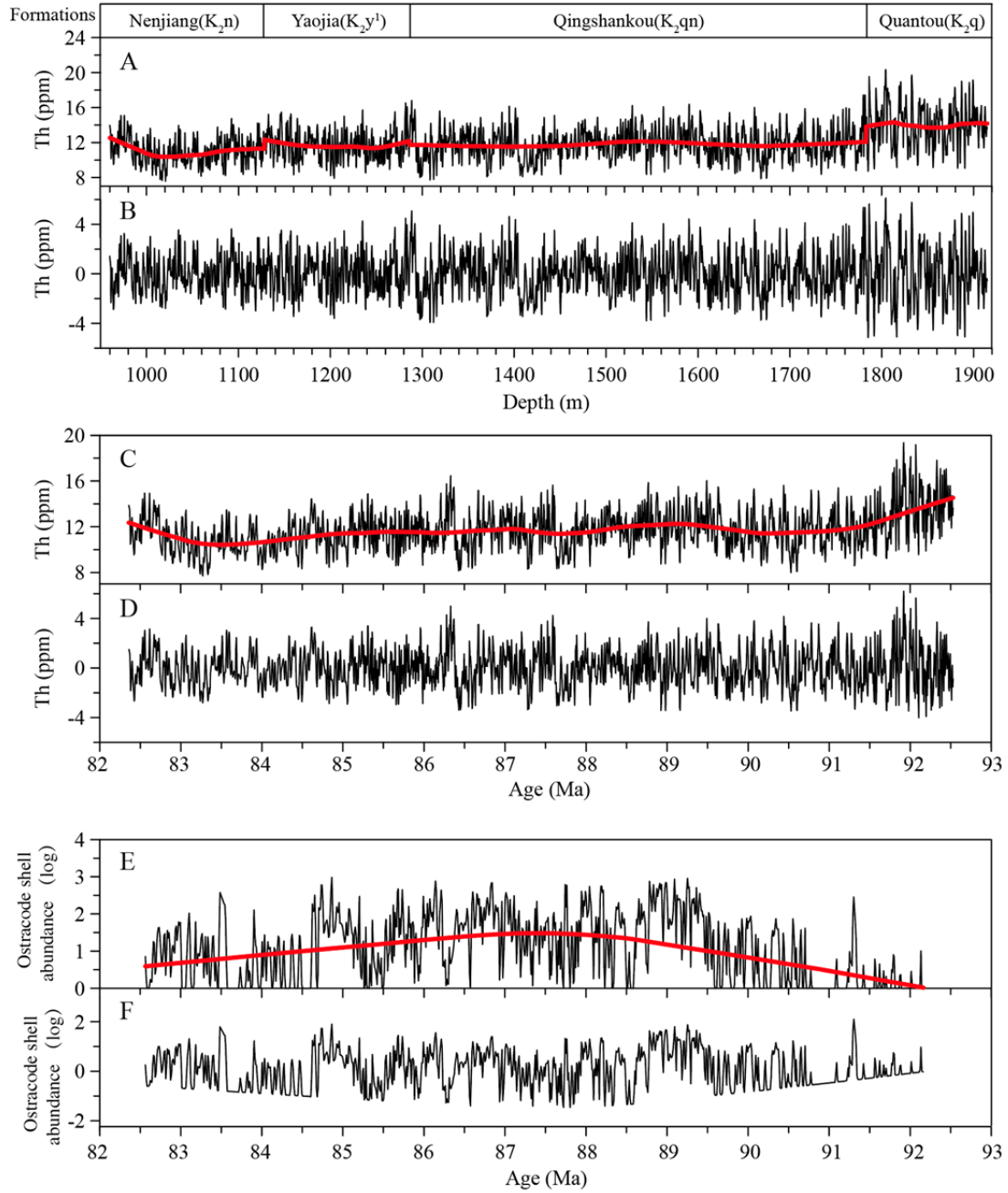


Figure S1. Long term trends in the Th and ostracode shell abundance series. A. The raw Th stratigraphic series (black) with the long-term 45% LOWESS trend (red). The detrending procedures were conducted on the four formations separately. B. The detrended Th stratigraphic series after subtracting the LOWESS trend shown in A. C. The 405-k.y. tuned Th time series (black) with the long-term 15% LOWESS trend (red). D. The 405-k.y. tuned Th time series after subtracting the LOWESS trend shown in C. E. The 405-k.y. tuned ostracode shell abundance time series (black) and 75% LOWESS trend (red). F. The 405-k.y. tuned ostracode shell abundance time series after subtracting the LOWESS trend shown in D. The total fraction of variance that was removed is ~13% for the Th data (C) and ~23% for the ostracode shell abundance data (E).

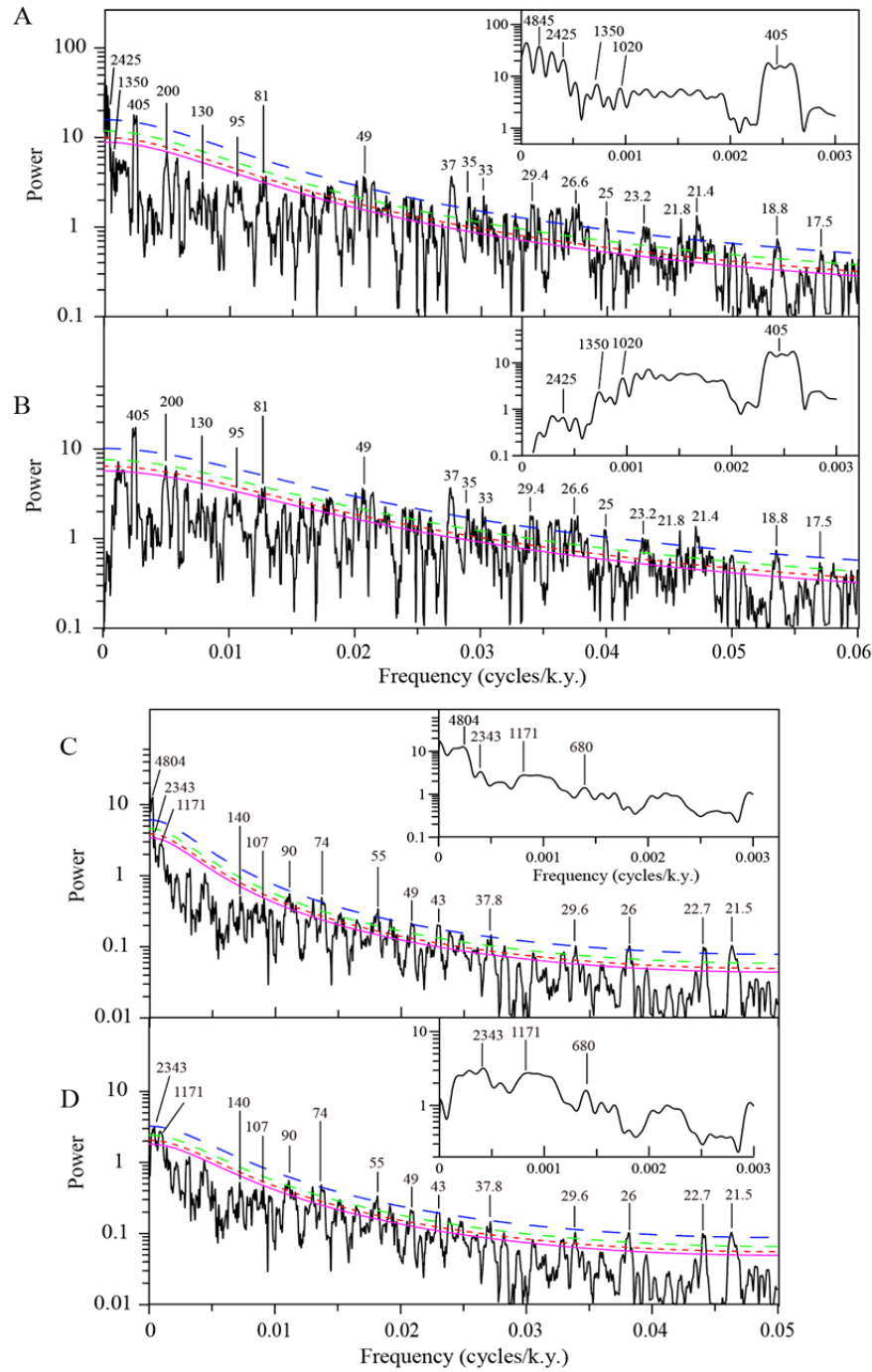


Figure S2. 2π multi-tapered power spectral analysis of paleoclimate proxy records from the SK-1s core in Songliao Basin, northeastern China. A. The 405-k.y. tuned raw Th time series. B. The 405-k.y. tuned detrended (see Fig. S1) Th time series. C. The 405-k.y. tuned raw ostracode shell abundance time series. D. The 405-k.y. tuned detrended (see Fig. S1) ostracode shell abundance time series. The pink, red, green and blue (dashed) curves represent 85%, 90%, 95% and 99% confidence levels for the exclusion of an AR(1) red noise model. Spectral peaks are labeled in k.y.

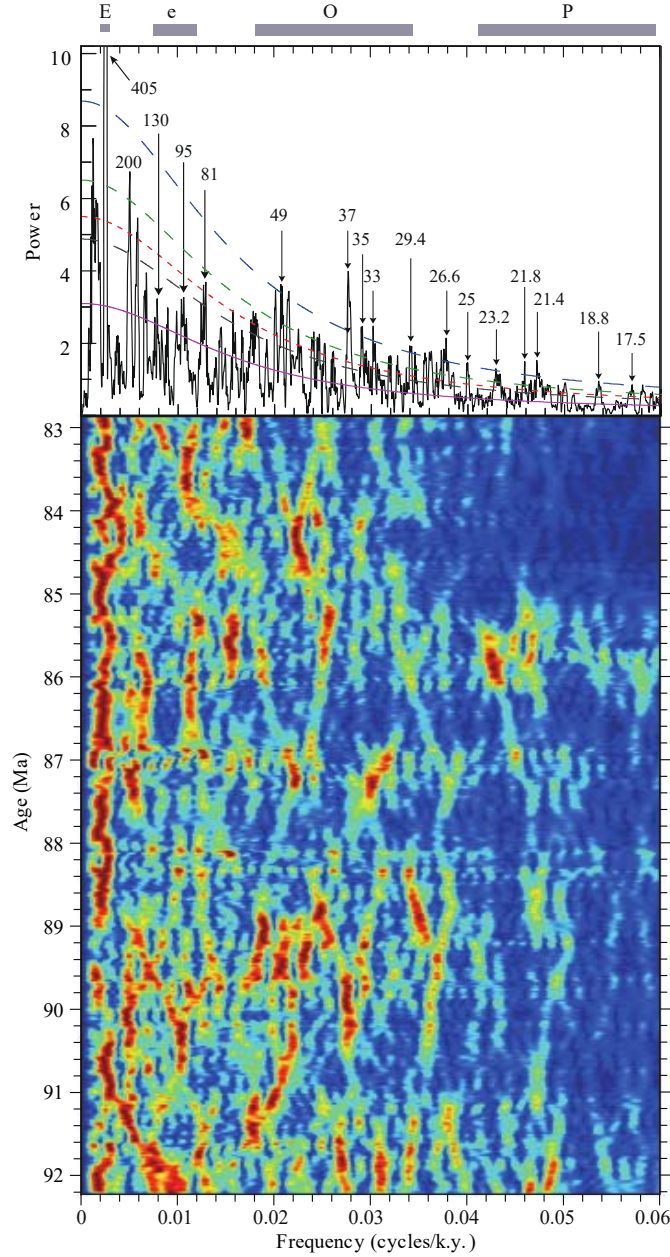


Figure S3. 2π multi-taper method (MTM) power spectrum (upper) and fast Fourier transform (FFT) spectrogram (lower) of 405-k.y.-tuned Th time series of the SK-1s core with an 800 k.y. sliding window and 5 k.y. step. The purple, gray, red, green and blue (dashed) curves represent the theoretical red noise spectrum, and 85%, 90%, 95% and 99% confidence levels. The peaks are labeled in k.y. The red and blue colors in FFT spectrogram represent high and low power, normalized to 1.

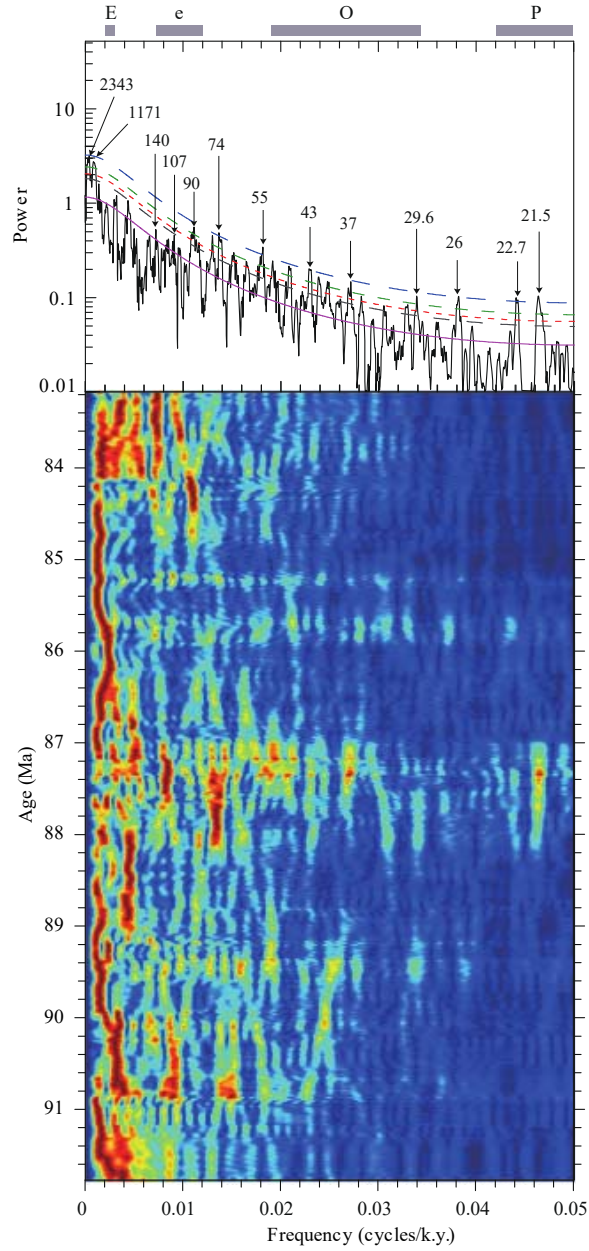


Figure S4. 2π multi-taper method (MTM) power spectrum (upper) and fast Fourier transform (FFT) spectrogram of 405-k.y.-tuned ostracode abundance time series, with a 1000 k.y. sliding window and 10 k.y. step. The purple, gray, red, green and blue (dashed) curves represent the theoretical red noise spectrum, and 85%, 90%, 95% and 99% confidence levels. The peaks are labeled in k.y. The red and blue colors in FFT spectrogram represent high and low power, normalized to 1.

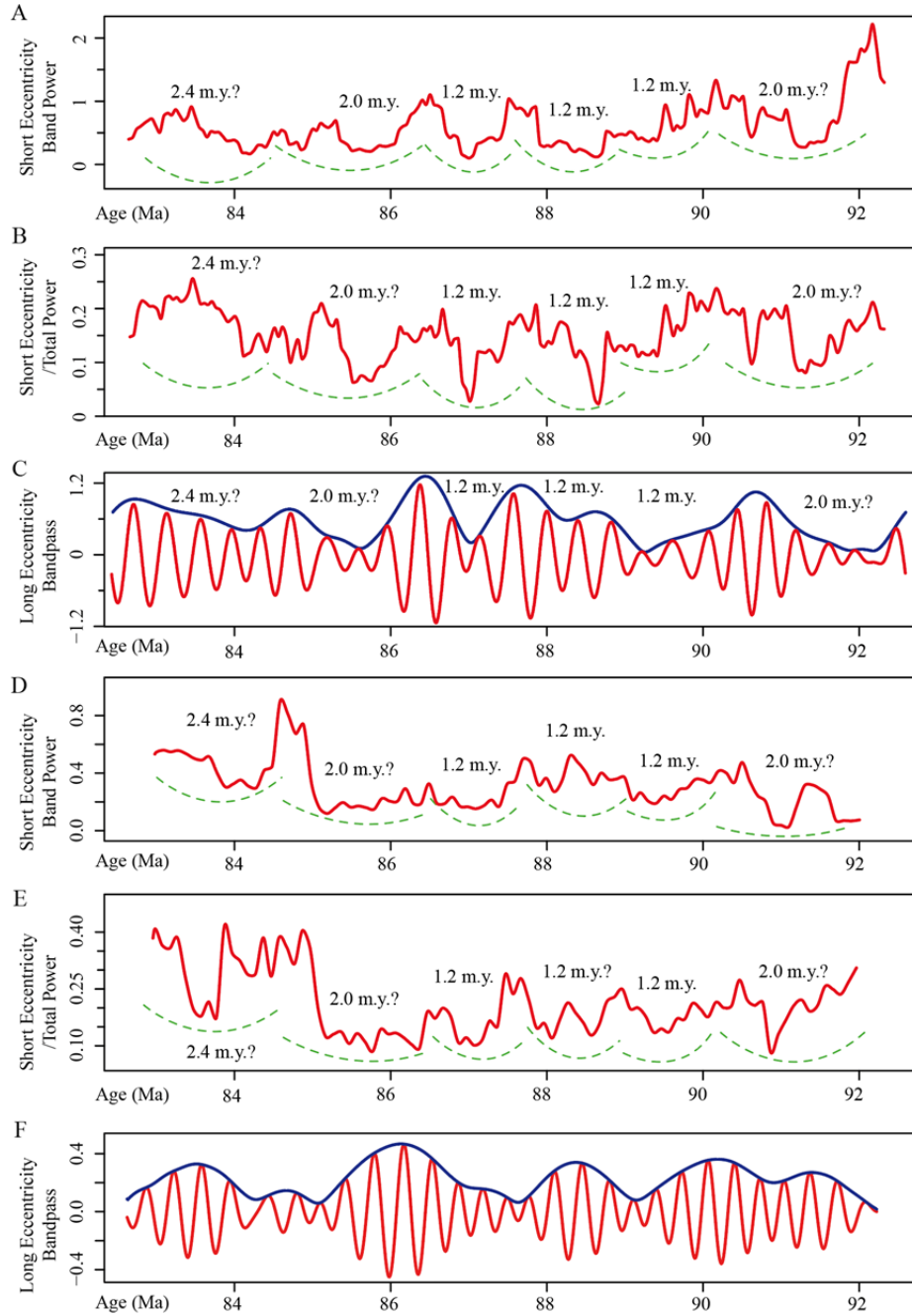


Figure S5. Comparison of amplitude modulations in the 405 k.y. tuned Th log and ostracode shell abundance time series at short and long orbital eccentricity frequencies. Short orbital eccentricity band power in the Th record (A) and ostracode abundance record (D), determined by integration of spectral power between 0.007 and 0.012 cycles/k.y. Short orbital eccentricity band power from (A, D) are normalized to total power (B, E), to provide an alternative assessment that compensates for secular changes in the sensitivity of sedimentation to Milankovitch-forced climate change. The amplitude modulation (blue curves) of the SK-1s 405-k.y. orbital eccentricity cycles of the Th (C) and ostracode shell abundance (F) filtered with passband of 0.002469 ± 0.001 cycles/k.y.

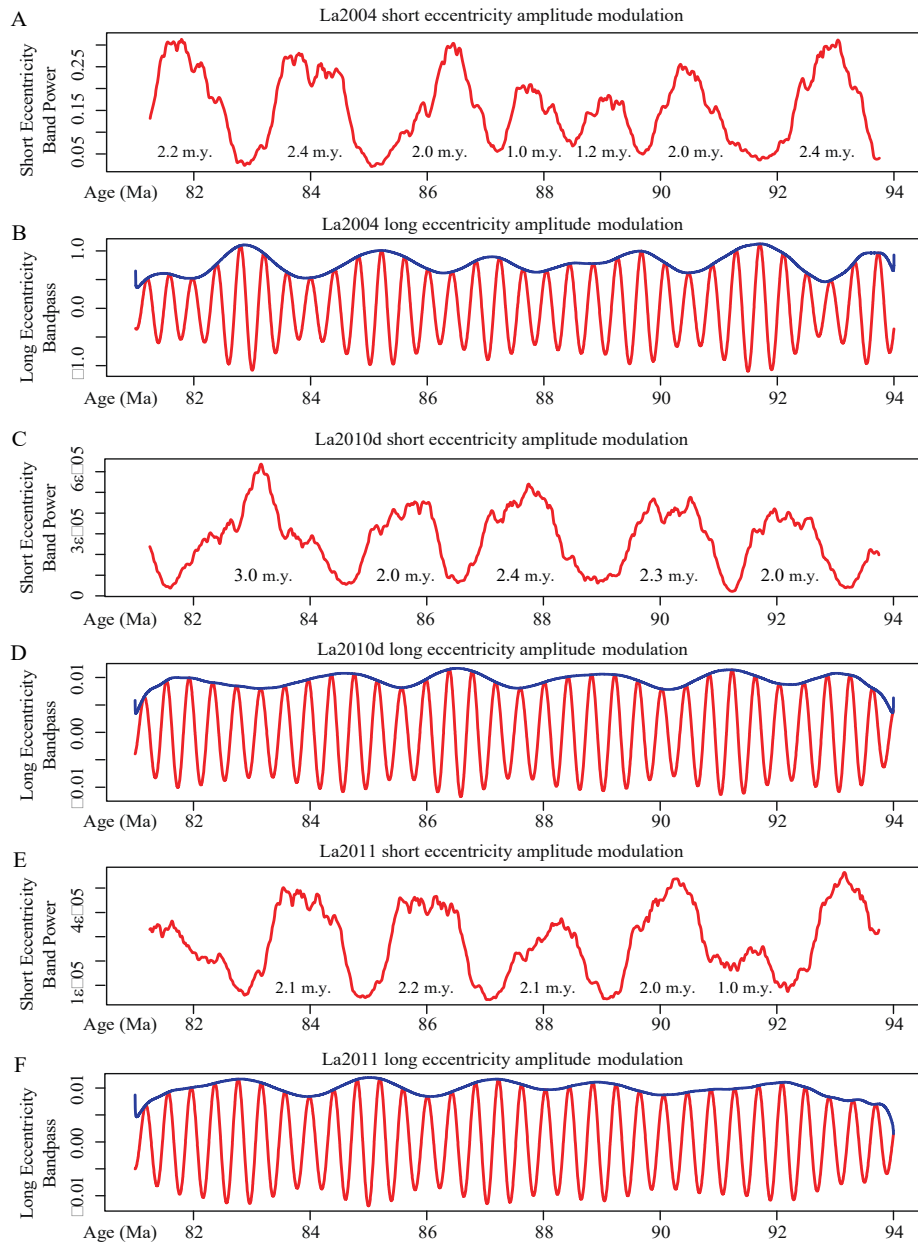


Figure S6. Amplitude modulations expressed in the short orbital eccentricity and 405-k.y. long orbital eccentricity time series from the theoretical astronomical solutions of La2004 (Laskar et al., 2004), La2010d (Laskar et al., 2011a) and La2011 (Laskar et al., 2011b). Short eccentricity band power in the solutions of (A) La2004, (C) La2010d and (E) La2011 solutions, were determined by integration of spectral power between 0.007 and 0.012 cycles/k.y. The amplitude modulations (blue curves) of the 405-k.y. long eccentricity cycles in the solutions of (B) La2004, (D) La2010d and (F) La2011, were determined by Hilbert Transform of the bandpass-filtered 405-k.y. long eccentricity signals (red curves; from 0.0015 cycles/k.y. to 0.0035 cycles/k.y.).

Table S1. Frequencies in Earth's short orbital eccentricity and obliquity variations influenced by secular frequencies s_3 , s_4 , g_3 and g_4 . Predicted values for 90 Ma assume $k = 53.0263264$ arcsec/year (Equation 40 in [Laskar et al. \(2004\)](#)); present-day $k = 50.475838$ arcsec/year, and present-day secular frequencies (in arcsec/year) $s_3 = -18.850$, $s_4 = -17.755$, $g_2 = 7.452$, $g_3 = 17.368$, $g_4 = 17.916$ and $g_5 = 4.257452$ (Table 3 in [Laskar et al. \(2004\)](#)). Actual values for these parameters at 90 Ma are embedded in the geologic record, and may not be the same as the prediction.

Astronomical parameter	Present-day (arcsec/year)	Present-day periodicity (year)	90 Ma (arcsec/year)	90 Ma periodicity (year)
$e_1=g_3-g_2$	9.909679	130,781	9.909679	130,781
$e_2=g_4-g_2$	10.456224	123,945	10.456224	123,945
$e_3=g_3-g_5$	13.109803	98,857	13.109803	98,857
$e_4=g_4-g_5$	13.651920	94,932	13.651920	94,932
$O_2=k+s_3$	31.626665	40,978	34.1763264	37,221
$O_3=k+s_4$	32.713667	39,616	35.2713264	36,744
$P_1=k+g_5$	54.73329	23,678	57.2837784	22,624
$P_2=k+g_2$	57.927838	22,372	60.4783264	21,429
$P_3=k+g_3$	67.843838	19,102	70.3943264	18,411
$P_4=k+g_4$	68.391838	18,949	70.9423264	18,268

Table S2. Phasing of La2004 solution, and SB (Th and ostracode shell abundance) and WIS (FMI) proxy modulations. For the e modulations, all three proxies are in phase with eccentricity maxima; for the O modulations, ostracode shell abundance is anti-phased with Th and FMI.

Modulation phase	Th (SB)	Ostracode shell abundance (SB)	FMI (WIS)
e maxima	high value, high clay	high abundance	low value, high clay
e minima	low value, low clay	low abundance	high value, low clay
O minima	high value, high clay	low abundance	low value, high clay
O maxima	low value, low clay	high abundance	high value, low clay

REFERENCES CITED

- Laskar, J., Fienga, A., Gastineau, M., and Manche, H., 2011a, La2010: a new orbital solution for the long-term motion of the Earth: *Astronomy Astrophysics*, v. 532, p. A89, <https://doi.org/10.1051/0004-6361/201116836>.
- Laskar, J., Gastineau, M., Delisle, J.-B., Farrés, A., and Fienga, A., 2011b, Strong chaos induced by close encounters with Ceres and Vesta: *Astronomy Astrophysics*, v. 532, p. L4, <https://doi.org/10.1051/0004-6361/201117504>.
- Laskar, J., Robutel, P., Joutel, F., Gastineau, M., Correia, A.C.M., and Levrard, B., 2004, A long-term numerical solution for the insolation quantities of the Earth: *Astronomy Astrophysics*, v. 428, p. 261–285, <https://doi.org/10.1051/0004-6361:20041335>.